

Machine Learning Accelerated Discovery of Corrosion-resistant High-entropy Alloys

Cheng Zeng^{*}, Andrew Neils, Jack Lesko, Nathan Post^{*}

The Roux Institute, Northeastern University, Portland, Maine, 04101, United States.

**Corresponding authors: Email: c.zeng@northeastern.edu and n.post@northeastern.edu, Tel: +1 401-396-6668 and +1 781-605-8671*

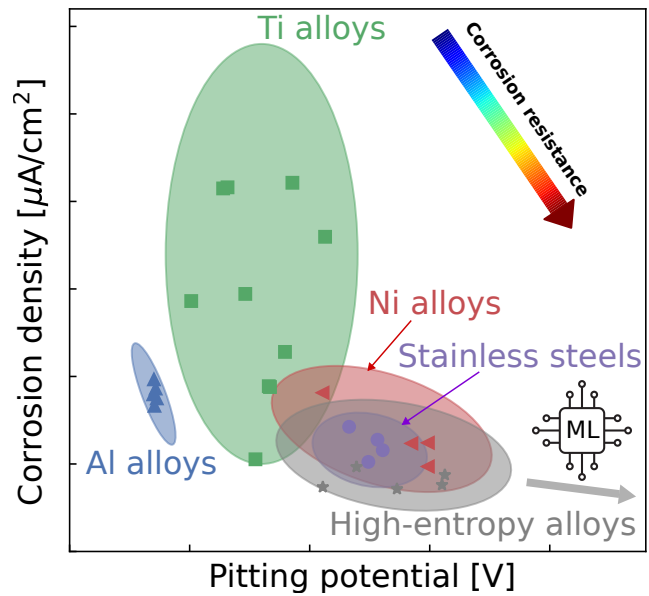
July 14, 2023

Abstract

Corrosion has a wide impact on society, causing catastrophic damage to structurally engineered components. An emerging class of corrosion-resistant materials are high-entropy alloys. However, high-entropy alloys live in high-dimensional composition and configuration space, making materials designs via experimental trial-and-error or brute-force ab initio calculations almost impossible. Here we develop a physics-informed machine-learning framework to identify corrosion-resistant high-entropy alloys. Three metrics are used to evaluate the corrosion resistance, including single-phase formability, surface energy and Pilling-Bedworth ratios. We used random forest models to predict the single-phase formability, trained on an experimental dataset. Machine learning inter-atomic potentials were employed to calculate surface energies and Pilling-Bedworth ratios, which are trained on first-principles data fast sampled using embedded atom models. A combination of random forest models and high-fidelity machine learning potentials represents the first of its kind to relate chemical compositions to corrosion resistance of high-entropy alloys, paving the way for automatic design of materials with superior corrosion protection. This framework was demonstrated on AlCrFeCoNi high-entropy alloys and we identified composition regions with high corrosion resistance. Machine learning predicted lattice constants and surface energies are consistent with values by first-principles calculations. The predicted single-phase formability and corrosion-resistant compositions of AlCrFeCoNi agree well with experiments. This framework is general in its application and applicable to other materials, enabling high-throughput screening of material candidates and potentially reducing the turnaround time for integrated computational materials engineering.

Keywords: High-entropy alloy, Corrosion protection, Machine learning potential, Random forest classification

Graphical TOC:



1 Introduction

High-entropy alloys are generally defined as alloys comprising no less than four elements and the percentage of each principal element is between 5 at.% and 35 at.%. The high-entropy concept was coined by Cantor [1] and Yeh [2] for equiatomic alloys with no less than five elements in 2004 almost the same time. The definition has been slightly extended to non-equimolar alloys with no less than four principal elements. This new class of materials has attracted increasing attention, found to display superior materials performance for mechanical properties [3–7], radiation resistance [8, 9] and corrosion resistance [10–12]. The high entropy of mixing usually leads to the formation of a disordered single phase for high-entropy alloys, such as face-centered cubic (FCC), body-centered cubic (BCC) and hexagonal closely-packed structures (HCP) [13, 14]. The homogeneous single phase improves passivity. In addition, high-entropy alloys can consist of elements with high passivation potency such as nickel, chromium, aluminum and titanium, leading to high pitting corrosion resistance.

Conventional corrosion-resistant alloys are mostly found by serendipity. Advances in physical theories, computational hardware and algorithms allow for rapid screening of candidate materials, paving the way for integrated computational materials engineering which aims to demystify the linkage between process, structure, property and performance. However, computational screening of corrosion-resistant alloys is challenging in that many factors can influence corrosion performance, including environmental conditions, chemical compositions and microstructures. Moreover, fundamental understanding of corrosion and various corrosion types adds more complexity to the material design. Recent works have been focused on building reliable databases for corrosion informatics, identifying reliable descriptors for corrosion performance and understanding the corrosion kinetics with multi-physics simulations [15–17]. Nyby et al. compiled a database for four types of alloys with an emphasis on six metrics used to describe their localized pitting corrosion [16]. Diao et al. collected a dataset for low-alloy steel and built machine learning models to predict their corrosion rate [18]. Roy et al. used machine learning algorithms to select the top three descriptors for prediction of the corrosion rates, including pH of the medium, halide concentration and composition of elements with the minimum reduction potential [19]. Taylor et al. identified a number of corrosion descriptors, such as cohesive energies, oxide formation energies and surface enrichment of passive elements, and related those descriptors to corrosion resistance with respect to surface passivation, dissolution and microstructure control [15]. Ke and Taylor reviewed the role of density functional theory (DFT) in modeling corrosion, and they pointed out corrosion metrics accessible by DFT, including oxygen and chloride adsorption energy, dissolution potential and surface energy [20]. Other computational methods based on peridynamics and phase-field modeling are often used to study the evolution of pitting corrosion [17, 21].

Unfortunately, the complexity of corrosion process makes it almost impossible to relate chemical compositions and microstructures of alloys directly to the corrosion performance. The vast composition and microstructure space of high-entropy alloys create complexity for the materials design problem. A workaround is multi-objective optimization based on empirical rules, which allows for screening material candidates with relative superior corrosion resistance. While some data-driven approaches and first-principles calculations exist to identify corrosion descriptors, the existing data-driven methods in nature lack physical insights and first-principles calculations are costly computationally. A physically meaningful and efficient approach to relating compositions with corrosion performance is still lacking. The objective of this work is to bridge the technical gap

for locating high-entropy alloys with potential high corrosion resistance in the high-dimensional composition space, in particular for pitting corrosion. We focused on pitting corrosion because the rate of localized pitting corrosion can be faster than uniform corrosion by orders of magnitude, hence pitting corrosion is more critical in applications where it exists [16]. It requires multi-scale and multi-physics simulations to understand the formation of passive film, passive film breakdown and pit growth stability [22], to the best of our knowledge not available. Pitting corrosion resistance is empirically associated with the ability of alloys to form a passive film, protectiveness of the passive film and pitting growth rate when the passive film breaks down. In this work, we chose three corrosion metrics considered to be influential to pitting corrosion, including *single phase formability*, *Pilling-Bedworth ratio* of passive elements, *surface energy*. A physics-informed machine learning framework was introduced to quantify the three corrosion metrics for a wide range of compositions of interested high-entropy alloys. The compositions with desired corrosion performances were identified by mapping out those corrosion metrics as a function of compositions. We tested this framework for AlCrFeCoNi high-entropy alloys because they belong to an emerging class of materials with superior mechanical properties and corrosion resistance [10, 23].

2 Theories and Methods

The key of this machine learning framework is to develop methods for quantification of three metrics relevant to pitting corrosion resistance. Machine learning models were trained to evaluate the three metrics for any arbitrary chemical compositions. Random forest classification models trained on experimental data were used to describe the single phase formability, whereas machine learning potentials trained on first-principles data were employed to calculate Pilling-Bedworth ratios and surface energies. In this section, we discuss in detail the qualitative relationship of the three metrics with pitting corrosion resistance and how to quantify each of them by machine learning models. The overall workflow of how to train the machine learning models is illustrated in Figure 1.

2.1 Single phase formability

The single phase formability was evaluated by a random forest classifier. It is crucial to form a homogeneous single phase for enhanced corrosion protection because it enhances passivity and prevents the fast galvanic corrosion. A physically rigorous approach to model single phase formability is thermodynamic modeling carried out with CALPHAD. The reliability of CALPHAD calculations is determined by the quality of experimental data as well as relevant first-principles calculations [24]. Instead of thermodynamic modeling, we used machine learning (ML) models trained on experimental data to predict the probability of forming single phases for an arbitrary given alloy composition. The experimental dataset are summarized by Yan et al. [25]. The workflow for single phase formability is shown in the top row of Figure 1. The raw data in total has 1807 entries and it takes input as the chemical compositions and output as the indicator for single phase formability. Single-phase alloys are labeled as '1', whereas multiple-phase alloys are labeled as '0'. It should be noted that phase formations are also dependent on the manufacturing processes and thermal history. It is assumed that most alloys in this experimental dataset are processed with similar techniques and environmental conditions, and the remaining exceptions represent outliers and noise in the dataset, whose impact on the robustness of ML models will be diminished by a cross-validation strategy due

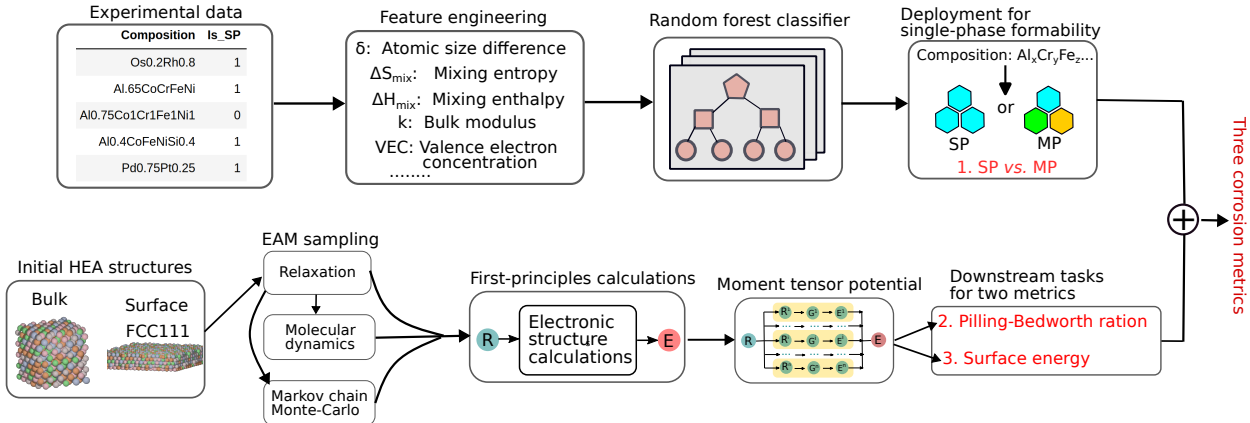


Figure 1: Workflow of machine learning accelerated discovery of corrosion-resistant high-entropy alloys.

to the averaging effect. Each input composition was converted to eight physical descriptors, as used by Yan et al [25], including atomic size difference, mixing enthalpy, mixing entropy, Pauli electronegativity difference, molar volume, bulk modulus, melting temperature and valence electron concentration. Next, random forest models were trained to relate the eight descriptors to the single phase formability. The trained random forest models are thus able to predict if alloys will form singl phase or multiple phases for a given composition. For the purpose of model validation, we held out 20% of the entire dataset for testing, which were used to examine the prediction accuracy of the final model on some unseen dataset, hence avoiding overfitting. Five-fold cross-validation was used on the remaining 80% dataset to tune the hyperparameters and to train the random forest classifier. The entire dataset was shuffled before splitting with a given random state to a test set and a data set for cross-validation, and ten random states were used to estimate uncertainties due to data splitting. Details of each descriptor, exploratory data analysis (Figure S1-S3), and hyperparameters of random forest models are included in the supporting information (SI).

2.2 Pilling-Bedworth ratio

The Pilling-Bedworth ratios and surface energies were quantified by machine learning potentials, which are trained following the procedure outlined in the bottom row of Figure 1. Pilling-Bedworth ratio (PBR) is used to describe the growth stress of an oxidation process. It describes the volume change due to oxidation right on an alloy surface, which follows Eq. (1) with respect to the oxidation of a metallic element B.

$$PBR_B = \frac{\text{Volume of a mole of } B_xO_y}{\text{Volume of } x \text{ moles of B in metal}} \quad (1)$$

It is well accepted that when $PBR < 1$, the formed oxide offers no protection to the alloy surface. If $1 \leq PBR \leq 2$, the oxide forms a passive layer and prevents structural alloys from direct corrosion although some compression stresses develop inside the oxide. When $PBR > 2$, the compression stresses become significant, causing the breakdown of the oxides. This simple analysis well explains that corrosion-resistant alloys typically contain Al, Zr, Ni, Ti, Fe or Cr whose PBR values are larger than 1 and not much larger than 2 [12, 26, 27].

When it comes to the oxidation of alloys, one or more elements may oxidize and form passive layers. Hence we need to identify elements that are thermodynamically preferential for oxidation. We can then calculate the PBR of the identified passive element by analyzing the volume change due to its oxidation. Xu and Gao introduced methods to compute PBR for the oxidation of alloys [28]. There are two possible cases for PBR values of alloys, depending on the relative diffusion rate of the passive element in alloys versus that in oxides. Generally the diffusion rate of passive elements within alloys are much faster relative to the rate within oxides so that alloy compositions near the surface can maintain a stoichiometry close to the original composition. For example, the diffusion coefficient of Cr in CrCrFeMnNi high-entropy alloys at 900 °C is about 10^{-12} cm²/s while self-diffusion of Cr in Cr₂O₃ has a coefficient on the order of 10^{-21} to 10^{-17} cm²/s [29, 30]. We recommend that readers consult the work of Xu and Gao [28] for calculation details of PBR for oxidation of alloys. For our benchmark material system AlCrFeCoNi, we examined the passivation of the Cr element although thermodynamic data, as tabulated in the SI, favors the formation of Al oxides over Cr oxides. Experimental data suggest that the addition of Al in CrFeCoNi alloys reduces passive film protection, implying that the major protection against pitting corrosion might be offered by the passivation of Cr [31]. Therefore, we consider the oxidation of Cr, which forms Cr₂O₃ with a mole weight of 102 g/mol and a density of 5.22 g/cm³. The volume of Cr in the alloy is calculated using a FCC crystal whose lattice parameters will be evaluated by machine learning potentials.

2.3 Surface energy

The role of crystallographic orientation and the corresponding surface energy in corrosion protection was first investigated by Song et al [32]. It is found that a densely packed surface with a lower surface energy could lead to a stronger bonding between surface atoms that impedes the dissolution of surface atoms to solutions. The electrochemical dissolution rate I_A of a metal ‘A’ with an exposed crystal plane (h,k,l) at a temperature T follows the relation:

$$I_{A,(h,k,l)} \propto \exp\left(\frac{\gamma_{(h,k,l)}}{RT}\right) \quad (2)$$

where R is the gas constant and $\gamma_{(h,k,l)}$ is the surface energy. Ramachandran and Nosonovsky found that a lower surface energy leads to a more hydrophobic surface, and hydrophobic surfaces tend to show higher corrosion resistance [33]. In this work, we used surface energy as a metric to describe the trend of average dissolution of atoms on the crystallographic plane FCC(111) of AlCrFeCoNi alloys with different compositions. It is arguable that a higher surface energy is associated with a higher average dissolution rate, resulting in faster pitting growth, although a more rigorous treatment may need to take into account sequential atom-by-atom dissolution on a metallic surface constrained by passive films formed on top of it, which we elected not to consider for the sake of simplicity. Surface energy of a facet reads as:

$$\gamma = \frac{E_{\text{slab}} - E_{\text{bulk}}}{2A} \quad (3)$$

where E_{slab} and E_{bulk} are respective potential energies of the FCC(111) facet and bulk cell, and A is the exposed area the facet. The bulk cells used to calculate surface energies are of L1₂ structures,

and the surface structures are the putative most stable structures found by Markov chain Monte-Carlo (MCMC) simulations. All items in Equ. 3 were found by atomistic modeling using machine learning potentials. The details of MCMC simulations are provided in the SI.

2.4 Machine learning potentials

Potential energy surfaces (PESs) represent one-to-one mappings between atomic positions ($\{R\}$) and potential energy (E) of a material system. PESs provide a plethora of information for material systems. For example, local minima on PESs represent stable states and the minimum energy trajectory connecting two local minima indicates a fundamental reaction pathway. The most often used methods to build reliable PESs are DFT calculations. However, standard DFT calculations are limited to hundreds of atoms due to the formidable $\mathcal{O}(M^{2-3})$ scaling with system sizes (M), such as numbers of basis sets, atoms or electrons [34]. It is thus computationally prohibitive to sample all points on *ab initio* PESs. One should note that DFT, first-principles and *ab initio* calculations are used interchangeably as they have the same meaning in this work. In the past decade, fitting *ab initio* PESs with machine learning (ML) algorithms have gained increasing momentum, and the ML-fitted PESs are termed machine learning potentials (MLP). Most MLPs relies on the nearsightedness principles [35], also known as *all chemistry is local*, implying that the total potential energy of a system with N atoms can be largely decomposed into a linear sum of all atomic contributions and each atomic contribution comes from the atom i interacting with neighboring atoms in a cutoff region, written as Eq. 4.

$$E = E(\{R\}) = \sum_{i=1}^N E_i = \sum_{i=1}^N E_i^{(\text{local})} \quad (4)$$

Thanks to and only because of the nearsightedness principle, MLPs can be trained with small-size first-principles data while allowing for reliable predictions on much larger systems [36]. It should be noted that the nearsightedness of first-principles calculations and machine learning algorithms should be well aligned to strike a good balance between computational efficiency and prediction accuracy [37]. A variety of ML algorithms have proven effective in fitting *ab initio* PESs, such as neural networks [36, 38], Gaussian process [39] and kernel ridge regression [40]. MLPs find applications in many fields, ranging from small molecules, to nanoparticle alloy catalysts and extended systems [41–43]. In this work, we employed a class of machine learning potentials termed moment tensor potentials (MTPs) for the high-entropy alloys which was found to be superior to other types of MLPs when tested on single-element systems by various simulation tasks [44]. Readers should refer to the work of Shapeev for implementation details of MTPs [45, 46]. MTPs were trained with systematically generated training data for high-entropy alloys AlCrFeCoNi, as outlined in the bottom row of Figure 1. We primed the algorithm with FCC bulk and surface structures. For each of the initial structures, the atomic position and lattice geometry are simultaneously optimized to find the stable structure, the process of which is termed structure optimization, also known as relaxation. The structure optimization used the embedded atom method (EAM) developed by Farkas and Caro [47]. Using EAM we also sampled a diverse pool of atomic configurations via molecular dynamics and Monte-Carlo simulations after the relaxed structures were found. The molecular dynamics simulations were used to perturb atomic positions, whereas the Monte-Carlo simulations were adopted to simulate exchange of two different atoms. Electronic structure calculations

with GPAW were performed to refine the energy and forces of selected EAM-sampled configurations [48]. Additionally, we carried out first-principles calculations for simple bulk and surface structures with numbers of elements ranging from one to five. Special quasi-random structures were generated using the tool in the alloy theoretic automated toolkit (ATAT) for simple bulk structures with more than two elements to best approximate a random solid solution [49, 50]. In total, 1569 first-principles structures were curated. We then trained MTPs upon those data, and we used the MTPs to carry out simulations needed for the evaluation of PBRs for the oxidation of Cr and surface energies of FCC(111) facets. Atomic structures were created and manipulated with the Atomic Simulation Environment (ASE) [51] and LAMMPS [52]. Computational settings of MTPs and GPAW calculations and details of the training data can be found in the SI. MTP enabled simulations to calculate relevant corrosion metrics are also elaborated in the SI. Scripts and notebooks for atomistic modeling and curation of training data will be supplied as a supporting dataset.

3 Results and discussion

3.1 Validation of ML models

ML models are often criticized for their poor transferability to data that are not existent in the training data set. As a result, it is of great importance to validate model performance before we deploy the models.

3.1.1 Random forest classifier

The experimental dataset used to train the random forest classifier includes in total 1807 entries. The 1807 data points were split to 80% and 20% for cross-validation and test, respectively. Hence 361 data points were used for testing, and ten different random states for the data splitting were used to obtain the standard deviation of model prediction accuracy on the test set. The random forest classifier gave a prediction accuracy of 89% on the test set with a standard deviation of 1%. The best model with the highest prediction accuracy was chosen for subsequent inferences. We also studied the feature importance using shapley values based on game theories [53]. Mixing entropy, atomic size difference and melting temperature were identified as the top three most important features, largely consistent with the work of Yan et al [25]. More feature importance results can be found in Figure S4 of SI.

3.1.2 Moment tensor potentials

The trained MTP gave ~ 5 meV/atom for the average absolute difference of energy and 0.058 eV/ \AA for the average absolute difference of atomic forces. To further validate the MTPs, we compared predicted lattice constants of single-element FCC crystals to values by DFT. We also compared the predicted surface energies of single-element FCC(111) facets with DFT. The comparison is summarized in Table. 1. One can see that MTP-predicted lattice constants are close to DFT calculations, with relative deviations around 1%. In terms of FCC(111) surface energies, although large deviations exist for elements Ni, Co and Al, the relative order of surface energy magnitude by MTP is in accordance with that by DFT.

Table 1: Lattice constants and FCC(111) surface energies for single-element structures: DFT *versus* MTP.

Element	Lattice constant [\AA]		Surface energy [J/m^2]	
	MTP	DFT	MTP	DFT
Al	4.08	4.04	0.77	0.86
Cr	3.62	3.62	2.61	2.65
Fe	3.44	3.46	2.49	2.45
Co	3.49	3.46	1.87	2.12
Ni	3.51	3.52	1.93	2.14

We also compared the phase stability among various single-crystal structures, including FCC random alloys (FCC_A1), FCC L1₂ ordered structures and BCC B2 structures. This comparison was used to test the ability of MTPs to predict the most stable phase of $\text{Al}_x(\text{CrFeNiCo})_{100-x}$ as a function Al compositions. Experimental observation and EAM-based calculations suggest that a low Al composition favors FCC-type phases while B2 phases are thermodynamically more stable at higher Al compositions [7, 47]. We calculated the cohesive energies of L1₂ and B2 for Al compositions up to 40%, with all Al in one sublattice and the remaining four elements randomly distributed. The FCC_A1 structures were generated by randomly placing the atoms in a FCC lattice. Figure 2 shows that at low Al contents (0–10%), L1₂ and FCC_A1 are both more stable than B2 phases. When Al compositions increase (10–20%), the ordered L1₂ becomes the most stable phase. In comparison, larger Al compositions (> 20%) favor the formation of ordered B2 phases, in good agreement with well-parameterized empirical potentials and experiments [7, 47]. The dashed line represents the most stable phases each Al composition. One should note that the first-principles data used to train MTPs only consist of FCC structures. Despite not seeing any BCC structures, the MTPs accurately predicted the trends of phase stability that are consistent with experiments and first-principles data, indicating decent transferability of the MTPs.

3.2 Effects of Al and Cr on relative corrosion resistance of AlCrFeCoNi

We examined the proposed machine learning framework by investigating the corrosion resistance of AlCrFeCoNi high-entropy alloys. This specific high-entropy system was used because of its superior corrosion performance and the availability of extensive experimental corrosion data, which can be compared to the predictions [10, 54, 55]. Nevertheless, the framework can be easily applied to other types of high-entropy alloys. We varied the compositions of Al and Cr while enforcing nearly equivalent compositions for the remaining Fe, Co and Ni elements. At each composition of the AlCrFeCoNi alloys, its single-phase formability was calculated by a random forest classifier and its Pilling-Bedworth ratio and surface energy were quantified by MTPs. Therefore, we mapped the three corrosion metrics as a function of AlCrFeCoNi compositions, based on which we can identify the compositions with relative high corrosion resistance. Al composition has a range of 0–25 at.%, and Cr composition is in the range of 10–30 at.% (see Figure 3). The lower bound for the Cr composition was set as 10% because Cr is the passive element, and a percolation model for passivation of alloys dictates that the smallest amount of elements to enable passivation is around 10% [56]. In other words, the alloy will only form continuous protective passive film with the passive element being of no less than 10%. For single-phase formability, the mesh grids of Al and

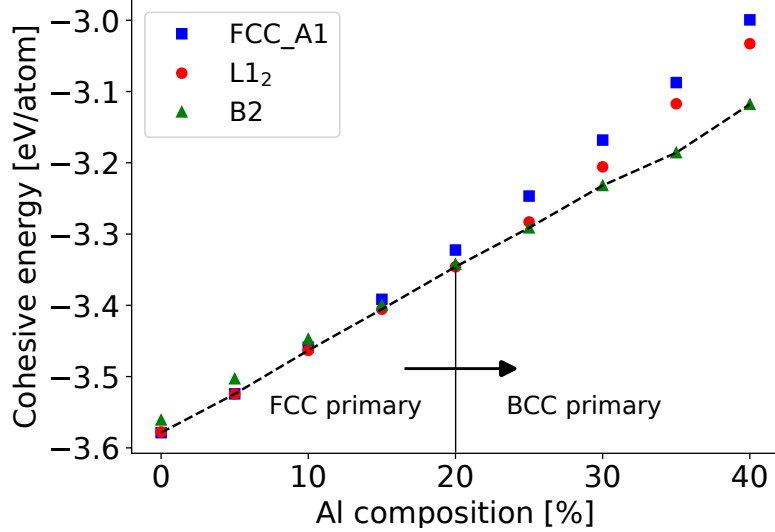


Figure 2: Cohesive energies of the FCC_A1, L1₂, and the ordered B2 phases for $\text{Al}_x(\text{CrFeCoNi})_{100-x}$ as a function of Al compositions. The most stable phases at all Al compositions are connected with dashed lines to guide the eyes.

Cr compositions both used an interval of 1% as the prediction by random forest classifier for each composition is fast and takes less than 1 second. For PBR_{Cr} , an interval of 5% for compositions of Al and Cr was used to quantify lattice parameters of L1₂ bulk cells using MTPs. Lattice parameters were then fitted by a linear function of Al and Cr compositions, with which lattice parameters for arbitrary Al and Cr compositions and corresponding volumes of Cr in the alloy can be estimated. The volume of Cr will be used to calculate PBR_{Cr} . In terms of surface energies, a composition interval of 5% was used to generate structures needed.

Figure 3(a) shows the results of single-phase formability. It can be seen that although some multiple-phase and single-phase training data are almost overlapped, the random forest classifier accurately predicts 91% of all training data listed in Figure 3(a). Besides, one can see a decision boundary at around 10% Al composition to separate single-phase alloys and multiple-phase alloys. The decision boundary is mostly determined by Al compositions and slightly associated with the Cr composition. An increased Cr composition will marginally shift the boundary to a lower Al composition. The trend of this decision boundary semi-quantitatively agrees with experimental data summarized by Wu et al [57], as indicated by the grey line in Figure 3(a). However, the prediction on the high Al composition region is confounded by the noisy training data, implying high prediction uncertainties in this region. In this regard, we are also interested in whether the single phase structure will be FCC or BCC structures since experiments found FCC crystals to be more resistant to pitting corrosion than BCC crystals [10, 55]. We identified the type of single phase to form for a given composition by comparing the cohesive energies of L1₂ and B2 phases following a similar procedure described in the validation of MTP. The results are plotted in Figure S5. Figure 3(a) and Figure S5 jointly show that FCC phases form at low Al and Cr compositions while BCC phases are more favorable at high Al and Cr compositions.

Figure 3(b) shows PBR_{Cr} for different Al and Cr compositions. Likewise, a major dependence on Al compositions and a minor dependence on Cr compositions can be identified. PBR_{Cr} values in the entire composition space studied have a lower bound of 2.00 and an upper bound of 2.18,

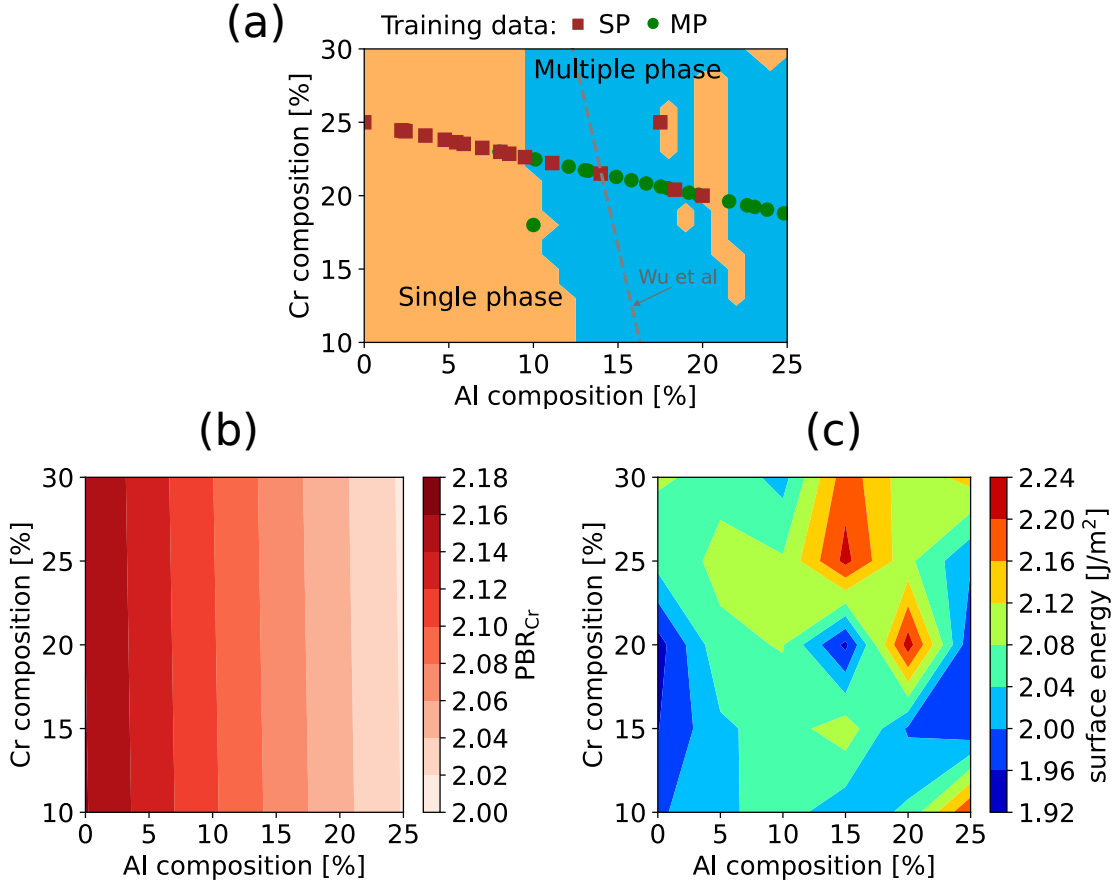


Figure 3: Single phase formability (a), Pilling-Bedworth ratios for oxidation of Cr (b) and FCC(111) surface energies (c) as a function of Al and Cr compositions in $\text{Al}_x\text{Cr}_y(\text{FeCoNi})_{100-x-y}$. The training data involving AlCrFeCoNi high-entropy alloys are included as scatter points in (a). Red squares and green circles in (a) represent single phase and multiple phase data, respectively. The grey dashed line in (a) is roughly the decision boundary by Wu et al [57].

both of which close to the PBR_{Cr} of pure Cr (2.04). In contrast, the surface energies exhibit much larger variations over compositions, ranging from 1.92 to 2.24 J/m². High surface energies are concentrated at the regions with high Al and Cr compositions, while low surface energies are found with Cr contents around 18% and with either low or high Al contents. To understand surface energy dependency on Al and Cr, we studied the surface segregation of Al and Cr for each composition, and the results are depicted in Figure S6. It is thus inferred that the low surface energies at the right-bottom region of Figure 3(c) originate from Al segregation and Cr depletion, probably because a Al FCC(111) surface has a much lower surface energy (0.77 J/m²) compared to a Cr FCC(111) surface (2.61 J/m²), as shown in Table 1. The Cr depletion on the surface lends itself difficult to formation of Cr₂O₃ passive films. Thus, highly corrosion-resistant AlCrFeCoNi alloys can potentially be found with low Al contents and around 18% Cr contents because the alloy with these compositions tend to form single-phase alloys and to exhibit low surface energies. The identified Al composition is consistent with experimental measurement [10, 31, 55].

4 Conclusion and outlook

A machine learning framework was proposed and developed to accelerate the discovery of corrosion-resistant high-entropy alloys. The physics-informed framework consists of two machine learning approaches. One approach uses experimental data to train random forest classifier for predictions of single phase formability. The other approach uses first-principles data to develop robust machine learning potentials, allowing for fast downstream simulations to obtain corrosion metrics such as Pilling-Bedworth ratio and surface energy. Current computational methods to understand corrosion performance of alloys mostly use pure statistical fitting or first-principles calculations. Unlike statistical fitting, the random forest classifier encodes meaningful physical knowledge into the feature engineering process. In comparison with first-principles calculations, the machine learning potentials can significantly mitigate the computational overhead of massive first-principles calculations. This framework was tested on a specific class of high-entropy alloys AlCrFeCoNi. The AlCrFeCoNi compositions were sampled by varying the Al and Cr compositions while enforcing the remaining Fe, Co and Ni compositions to be almost identical. The three corrosion metrics were evaluated on those sampled compositions, based on which the desired compositions for corrosion protection were identified. We found that low Al compositions and around 18% Cr compositions tend to form corrosion-resistant alloys, in satisfactory agreement with experimental observations. Although additional corrosion descriptors, such as cohesive energy, and adsorption energy of oxygen and chloride, may be needed to provide a more comprehensive description of corrosion performance, the three simple corrosion metrics used in this work have proved to be effective in narrowing down the composition space for further selection.

Our scheme is not limited to AlCrFeCoNi high-entropy alloys and corrosion properties. The methodology can be easily adapted for other material applications where the relationship of chemical compositions with properties is sought after and where ML accelerated molecular simulations are indispensable for high-throughput screening of material candidates. For instance, ductility of alloys can be evaluated by stacking fault energies which can be calculated by using MLPs, and hardness can be estimated using machine learning regression on experimental dataset [58, 59]. One should note that most state-of-the-art machine learning potentials use element-specific features, which limit the transferability of MLPs. In other words, MLPs trained on certain elements can-

not be applied to elements not existing in the training data. Moreover, a large amount of training structures are required to build reliable ML models for high-entropy systems. Developing a robust element-agnostic featurization method, and reducing numbers of representative images and features are promising future directions. Element-agnostic featurization methods are just emerging in recent years and needs further development. For example, there are methods using multipole expansions of the electron density around atoms [60] or graph representation of materials [61]. Current image and feature selection methods use linear correlations in the feature space [62]. More advanced methods may require understand the complex non-linear mapping between features and outputs (e.g. energy and forces).

SUPPORTING INFORMATION

Standard enthalpy of formation for oxides of certain metals, Computational settings of DFT calculations, Details of moment tensor potential (MTP), Random forest classifier for single phase formability, Fast sampling of configurations using the embedded atom method (EAM), First-principles data for MTP, MTP-enabled simulations for corrosion metrics, and Supporting results are included in the supporting information.

DATA AND CODE AVAILABILITY

All scripts and notebooks for simulation tasks and data analytics are saved in a private repository and will be publicized after this manuscript is accepted for publication. Data generated in this work are available from the corresponding authors upon reasonable requests.

AUTHOR INFORMATION

Corresponding authors. *Email: c.zeng@northeastern.edu and n.post@northeastern.edu, Telephone +1 401-396-6668 and +1 781-605-8671.

Acknowledgments. This work was completed in part using the Discovery cluster, supported by the Research Computing team at Northeastern University. Cheng Zeng is grateful for the financial support by Alfond Post Doc Research Fellowship. We thank Dr. Liang Qi (University of Michigan) for providing valuable technical feedback to our poster presented at ICME2023 conference in Orlando, Florida, USA.

References

- [1] Cantor, B.; Chang, I.T.H.; Knight, P.; Vincent, A.J.B. Microstructural development in equiatomic multicomponent alloys. *Materials Science and Engineering: A* **2004**; 375-377, 213–218.
- [2] Yeh, J.W.; Chen, S.K.; Lin, S.J.; Gan, J.Y.; Chin, T.S.; Shun, T.T.; Tsau, C.H.; Chang, S.Y. Nanostructured High-Entropy Alloys with Multiple Principal Elements: Novel Alloy Design Concepts and Outcomes. *Advanced Engineering Materials* **2004**; 6, 299–303.

[3] Gludovatz, B.; Hohenwarter, A.; Catoor, D.; Chang, E.H.; George, E.P.; Ritchie, R.O. A fracture-resistant high-entropy alloy for cryogenic applications. *Science* **2014**; 345, 1153–1158.

[4] Yang, T.; Zhao, Y.L.; Tong, Y.; Jiao, Z.B.; Wei, J.; Cai, J.X.; Han, X.D.; Chen, D.; Hu, A.; Kai, J.J.; Lu, K.; Liu, Y.; Liu, C.T. Multicomponent intermetallic nanoparticles and superb mechanical behaviors of complex alloys. *Science* **2018**; 362, 933–937.

[5] Li, Z.; Pradeep, K.G.; Deng, Y.; Raabe, D.; Tasan, C.C. Metastable high-entropy dual-phase alloys overcome the strength–ductility trade-off. *Nature* **2016**; 534, 227–230.

[6] Ding, Z.Y.; Cao, B.X.; Luan, J.H.; Jiao, Z.B. Synergistic effects of Al and Ti on the oxidation behaviour and mechanical properties of L12-strengthened FeCoCrNi high-entropy alloys. *Corrosion Science* **2021**; 184, 109365.

[7] Wang, W.R.; Wang, W.L.; Wang, S.C.; Tsai, Y.C.; Lai, C.H.; Yeh, J.W. Effects of Al addition on the microstructure and mechanical property of Al_xCoCrFeNi high-entropy alloys. *Intermetallics* **2012**; 26, 44–51.

[8] Kumar, N.A.P.K.; Li, C.; Leonard, K.J.; Bei, H.; Zinkle, S.J. Microstructural stability and mechanical behavior of FeNiMnCr high entropy alloy under ion irradiation. *Acta Materialia* **2016**; 113, 230–244.

[9] Lu, Y.; Huang, H.; Gao, X.; Ren, C.; Gao, J.; Zhang, H.; Zheng, S.; Jin, Q.; Zhao, Y.; Lu, C.; Wang, T.; Li, T. A promising new class of irradiation tolerant materials: Ti₂ZrHfV_{0.5}Mo_{0.2} high-entropy alloy. *Journal of Materials Science & Technology* **2019**; 35, 369–373.

[10] Shi, Y.; Collins, L.; Feng, R.; Zhang, C.; Balke, N.; Liaw, P.K.; Yang, B. Homogenization of Al_xCoCrFeNi high-entropy alloys with improved corrosion resistance. *Corrosion Science* **2018**; 133, 120–131.

[11] Qiu, Y.; Gibson, M.A.; Fraser, H.L.; Birbilis, N. Corrosion characteristics of high entropy alloys. *Materials Science and Technology* **2015**; 31, 1235–1243.

[12] Fu, Y.; Li, J.; Luo, H.; Du, C.; Li, X. Recent advances on environmental corrosion behavior and mechanism of high-entropy alloys. *Journal of Materials Science & Technology* **2021**; 80, 217–233.

[13] Steurer, W. Single-phase high-entropy alloys – A critical update. *Materials Characterization* **2020**; 162, 110179.

[14] Zhao, Y.J.; Qiao, J.W.; Ma, S.G.; Gao, M.C.; Yang, H.J.; Chen, M.W.; Zhang, Y. A hexagonal close-packed high-entropy alloy: The effect of entropy. *Materials & Design* **2016**; 96, 10–15.

[15] Taylor, C.D.; Lu, P.; Saal, J.; Frankel, G.S.; Scully, J.R. Integrated computational materials engineering of corrosion resistant alloys. *npj Mater Degrad* **2018**; 2, 1–10.

[16] Nyby, C.; Guo, X.; Saal, J.E.; Chien, S.C.; Gerard, A.Y.; Ke, H.; Li, T.; Lu, P.; Oberdorfer, C.; Sahu, S.; Li, S.; Taylor, C.D.; Windl, W.; Scully, J.R.; Frankel, G.S. Electrochemical metrics for corrosion resistant alloys. *Sci Data* **2021**; 8, 58.

[17] Ansari, T.Q.; Huang, H.; Shi, S.Q. Phase field modeling for the morphological and microstructural evolution of metallic materials under environmental attack. *npj Comput Mater* **2021**; 7, 1–21.

[18] Diao, Y.; Yan, L.; Gao, K. Improvement of the machine learning-based corrosion rate prediction model through the optimization of input features. *Materials & Design* **2021**; 198, 109326.

[19] Roy, A.; Taufique, M.F.N.; Khakurel, H.; Devanathan, R.; Johnson, D.D.; Balasubramanian, G. Machine-learning-guided descriptor selection for predicting corrosion resistance in multi-principal element alloys. *npj Mater Degrad* **2022**; 6, 1–10.

[20] Ke, H.; Taylor, C.D. Density Functional Theory: An Essential Partner in the Integrated Computational Materials Engineering Approach to Corrosion. *Corrosion* **2019**; 75, 708–726.

[21] Chen, Z.; Jafarzadeh, S.; Zhao, J.; Bobaru, F. A coupled mechano-chemical peridynamic model for pit-to-crack transition in stress-corrosion cracking. *Journal of the Mechanics and Physics of Solids* **2021**; 146, 104203.

[22] Li, T.; Wu, J.; Frankel, G.S. Localized corrosion: Passive film breakdown vs. Pit growth stability, Part VI: Pit dissolution kinetics of different alloys and a model for pitting and repassivation potentials. *Corrosion Science* **2021**; 182, 109277.

[23] Ren, J.; Zhang, Y.; Zhao, D.; Chen, Y.; Guan, S.; Liu, Y.; Liu, L.; Peng, S.; Kong, F.; Poplawsky, J.D.; Gao, G.; Voisin, T.; An, K.; Wang, Y.M.; Xie, K.Y.; Zhu, T.; Chen, W. Strong yet ductile nanolamellar high-entropy alloys by additive manufacturing. *Nature* **2022**; 608, 62–68.

[24] Mao, H.; Chen, H.L.; Chen, Q. TCHEA1: A Thermodynamic Database Not Limited for “High Entropy” Alloys. *J. Phase Equilib. Diffus.* **2017**; 38, 353–368.

[25] Yan, Y.; Lu, D.; Wang, K. Accelerated discovery of single-phase refractory high entropy alloys assisted by machine learning. *Computational Materials Science* **2021**; 199, 110723.

[26] Zeng, C.; Ling, Y.; Bai, Y.; Zhang, R.; Dai, X.; Chen, Y. Hydrogen permeation characteristic of nanoscale passive films formed on different zirconium alloys. *International Journal of Hydrogen Energy* **2016**; 41, 7676–7690.

[27] Zeng, C.; Bai, Y.; Ling, Y.; Xin, Z.; Liang, H.; Deng, X. Hydrogen interaction characteristic of nanoscale oxide films grown on iron–nickel based stainless steel by selective thermal oxidation. *International Journal of Hydrogen Energy* **2017**; 42, 20910–20921.

[28] Xu, C.; Gao, W. Pilling-Bedworth ratio for oxidation of alloys. *Materials Research Innovations* **2000**; 3, 231–235.

[29] Sabioni, A.C.S.; Huntz, A.M.; Silva, F.; Jomard, F. Diffusion of iron in Cr₂O₃: polycrystals and thin films. *Materials Science and Engineering: A* **2005**; 392, 254–261.

[30] Tsai, K.Y.; Tsai, M.H.; Yeh, J.W. Sluggish diffusion in Co–Cr–Fe–Mn–Ni high-entropy alloys. *Acta Materialia* **2013**; 61, 4887–4897.

- [31] Shi, Y.; Yang, B.; Rack, P.D.; Guo, S.; Liaw, P.K.; Zhao, Y. High-throughput synthesis and corrosion behavior of sputter-deposited nanocrystalline Al_x(CoCrFeNi)100-x combinatorial high-entropy alloys. *Materials & Design* **2020**; 195, 109018.
- [32] Song, G.L.; Mishra, R.; Xu, Z. Crystallographic orientation and electrochemical activity of AZ31 Mg alloy. *Electrochemistry Communications* **2010**; 12, 1009–1012.
- [33] Ramachandran, R.; Nosonovsky, M. Coupling of surface energy with electric potential makes superhydrophobic surfaces corrosion-resistant. *Phys. Chem. Chem. Phys.* **2015**; 17, 24988–24997.
- [34] Bowler, D.R.; Miyazaki, T. $\mathcal{O}(N)$ methods in electronic structure calculations. *Reports on Progress in Physics* **2012**; 75, 036503.
- [35] Kohn, W. Density Functional and Density Matrix Method Scaling Linearly with the Number of Atoms. *Physical Review Letters* **1996**; 76, 3168–3171.
- [36] Behler, J.; Parrinello, M. Generalized Neural-Network Representation of High-Dimensional Potential-Energy Surfaces. *Physical Review Letters* **2007**; 98, 146401.
- [37] Zeng, C.; Chen, X.; Peterson, A.A. A nearsighted force-training approach to systematically generate training data for the machine learning of large atomic structures. *The Journal of Chemical Physics* **2022**; 156, 064104.
- [38] Xie, T.; Grossman, J.C. Crystal Graph Convolutional Neural Networks for an Accurate and Interpretable Prediction of Material Properties. *Physical Review Letters* **2018**; 120, 145301. Publisher: American Physical Society.
- [39] Bartók, A.P.; Payne, M.C.; Kondor, R.; Csányi, G. Gaussian Approximation Potentials: the accuracy of quantum mechanics, without the electrons. *Physical Review Letters* **2010**; 104, 136403.
- [40] Rupp, M.; Tkatchenko, A.; Müller, K.R.; von Lilienfeld, O.A. Fast and Accurate Modeling of Molecular Atomization Energies with Machine Learning. *Physical Review Letters* **2012**; 108, 058301.
- [41] Batzner, S.; Musaelian, A.; Sun, L.; Geiger, M.; Mailoa, J.P.; Kornbluth, M.; Molinari, N.; Smidt, T.E.; Kozinsky, B. E(3)-equivariant graph neural networks for data-efficient and accurate interatomic potentials. *Nat Commun* **2022**; 13, 2453.
- [42] Zeng, C.; Sahoo, S.J.; Medford, A.J.; Peterson, A.A. The phase stability of large-size nanoparticle alloy catalysts at ab initio quality using a nearsighted force-training approach **2023**.
- [43] Behler, J.; Csányi, G. Machine learning potentials for extended systems: a perspective. *Eur. Phys. J. B* **2021**; 94, 142.
- [44] Zuo, Y.; Chen, C.; Li, X.; Deng, Z.; Chen, Y.; Behler, J.; Csányi, G.; Shapeev, A.V.; Thompson, A.P.; Wood, M.A.; Ong, S.P. Performance and Cost Assessment of Machine Learning Interatomic Potentials. *J. Phys. Chem. A* **2020**; 124, 731–745.

[45] Shapeev, A.V. Moment Tensor Potentials: A Class of Systematically Improvable Interatomic Potentials. *Multiscale Model. Simul.* **2016**; 14, 1153–1173.

[46] Novikov, I.S.; Gubaev, K.; Podryabinkin, E.V.; Shapeev, A.V. The MLIP package: moment tensor potentials with MPI and active learning. *Mach. Learn.: Sci. Technol.* **2020**; 2, 025002. Publisher: IOP Publishing.

[47] Farkas, D.; Caro, A. Model interatomic potentials for Fe–Ni–Cr–Co–Al high-entropy alloys. *Journal of Materials Research* **2020**; 35, 3031–3040.

[48] Dohn, A.O.; Jónsson, E.Ö.; Levi, G.; Mortensen, J.J.; Lopez-Acevedo, O.; Thygesen, K.S.; Jacobsen, K.W.; Ulstrup, J.; Henriksen, N.E.; Møller, K.B.; Jónsson, H. Grid-Based Projector Augmented Wave (GPAW) Implementation of Quantum Mechanics/Molecular Mechanics (QM/MM) Electrostatic Embedding and Application to a Solvated Diplatinum Complex. *Journal of Chemical Theory and Computation* **2017**; 13, 6010–6022.

[49] Zunger, A.; Wei, S.H.; Ferreira, L.G.; Bernard, J.E. Special quasirandom structures. *Phys. Rev. Lett.* **1990**; 65, 353–356.

[50] van de Walle, A.; Tiwary, P.; de Jong, M.; Olmsted, D.L.; Asta, M.; Dick, A.; Shin, D.; Wang, Y.; Chen, L.Q.; Liu, Z.K. Efficient stochastic generation of special quasirandom structures. *Calphad* **2013**; 42, 13–18.

[51] Hjorth Larsen, A.; Jørgen Mortensen, J.; Blomqvist, J.; Castelli, I.E.; Christensen, R.; Dułak, M.; Friis, J.; Groves, M.N.; Hammer, B.; Hargus, C.; Hermes, E.D.; Jennings, P.C.; Bjerre Jensen, P.; Kermode, J.; Kitchin, J.R.; Leonhard Kolsbjerg, E.; Kubal, J.; Kaasbjerg, K.; Lysgaard, S.; Bergmann Maronsson, J.; Maxson, T.; Olsen, T.; Pastewka, L.; Peterson, A.; Rostgaard, C.; Schiøtz, J.; Schütt, O.; Strange, M.; Thygesen, K.S.; Vegge, T.; Vilhelmsen, L.; Walter, M.; Zeng, Z.; Jacobsen, K.W. The atomic simulation environment—a Python library for working with atoms. *Journal of Physics: Condensed Matter* **2017**; 29, 273002.

[52] Thompson, A.P.; Aktulga, H.M.; Berger, R.; Bolintineanu, D.S.; Brown, W.M.; Crozier, P.S.; in 't Veld, P.J.; Kohlmeyer, A.; Moore, S.G.; Nguyen, T.D.; Shan, R.; Stevens, M.J.; Tranchida, J.; Trott, C.; Plimpton, S.J. LAMMPS - a flexible simulation tool for particle-based materials modeling at the atomic, meso, and continuum scales. *Computer Physics Communications* **2022**; 271, 108171.

[53] Merrick, L.; Taly, A. The Explanation Game: Explaining Machine Learning Models Using Shapley Values. In A. Holzinger; P. Kieseberg; A.M. Tjoa; E. Weippl, eds., *Machine Learning and Knowledge Extraction*, Lecture Notes in Computer Science. Springer International Publishing, Cham. ISBN 978-3-030-57321-8, pp. 17–38.

[54] Shi, H.; Jianu, A.; Fetzer, R.; Szabó, D.V.; Schlabach, S.; Weisenburger, A.; Tang, C.; Heinzel, A.; Lang, F.; Müller, G. Compatibility and microstructure evolution of Al–Cr–Fe–Ni high entropy model alloys exposed to oxygen-containing molten lead. *Corrosion Science* **2021**; 189, 109593.

[55] Shi, Z.J.; Wang, Z.B.; Wang, X.D.; Zhang, S.; Zheng, Y.G. Effect of thermally induced B2 phase on the corrosion behavior of an Al0.3CoCrFeNi high entropy alloy. *Journal of Alloys and Compounds* **2022**; 903, 163886.

[56] Sieradzki, K.; Newman, R.C. A Percolation Model for Passivation in Stainless Steels. *J. Electrochem. Soc.* **1986**; 133, 1979.

[57] Wu, Q.; Wang, Z.; Hu, X.; Zheng, T.; Yang, Z.; He, F.; Li, J.; Wang, J. Uncovering the eutectics design by machine learning in the Al–Co–Cr–Fe–Ni high entropy system. *Acta Materialia* **2020**; 182, 278–286.

[58] Hu, Y.J.; Sundar, A.; Ogata, S.; Qi, L. Screening of generalized stacking fault energies, surface energies and intrinsic ductile potency of refractory multicomponent alloys. *Acta Materialia* **2021**; 210, 116800.

[59] Yang, C.; Ren, C.; Jia, Y.; Wang, G.; Li, M.; Lu, W. A machine learning-based alloy design system to facilitate the rational design of high entropy alloys with enhanced hardness. *Acta Materialia* **2022**; 222, 117431.

[60] Lei, X.; Medford, A.J. A Universal Framework for Featurization of Atomistic Systems. *J. Phys. Chem. Lett.* **2022**; 13, 7911–7919.

[61] Chen, C.; Ong, S.P. A universal graph deep learning interatomic potential for the periodic table. *Nat Comput Sci* **2022**; 2, 718–728.

[62] Imbalzano, G.; Anelli, A.; Giofré, D.; Klees, S.; Behler, J.; Ceriotti, M. Automatic selection of atomic fingerprints and reference configurations for machine-learning potentials. *The Journal of Chemical Physics* **2018**; 148, 241730.

Supporting Information

Machine Learning Accelerated Discovery of Corrosion-resistant High-entropy Alloys

Cheng Zeng*, Andrew Neils, Jack Lesko, Nathan Post*

The Roux Institute, Northeastern University, Portland, Maine, 04101, United States.

*Corresponding authors: Email: c.zeng@northeastern.edu and n.post@northeastern.edu, Tel: +1 401-396-6668 and +1 781-605-8671

This Supporting Information (SI) includes standard enthalpy of formation for oxides of certain metals, Computational settings of DFT calculations, Details of moment tensor potential (MTP), Random forest classifier for single phase formability, Fast sampling of configurations using the embedded atom method (EAM), First-principles data for MTP, MTP-enabled simulations for corrosion metrics, and Supporting results.

S-1 Standard enthalpy of formation of oxides

Table S1 summarized the enthalpy of formation of oxides at room temperature (298.15 K). Data are found on NIST Chemistry WebBook. One should note that one mole of Cr_2O_3 and Al_2O_3 includes two moles of Cr and Al. Therefore, a fair comparison between formation enthalpies of different oxides needs to divide the formation enthalpy by the number of metal element.

S-2 Computational settings for DFT calculations

Grid-based projector-augmented wave code (GPAW) was used for all DFT calculations [1]. The Generalized Gradient Approximation (GGA) exchange-correlation functional parameterized by

Table S1: Molar enthalpy of oxide formation for Al, Cr, Fe, Co and Ni. Data are excerpted from [NIST Chemistry Webbook](#).

Oxide	$\Delta_f H_{\text{solid}}^0$ [kJ/mol]
Al_2O_3	-1675.7
Cr_2O_3	-1134.70
FeO	-272.04
CoO	-237.74
NiO	-239.7

Perdew-Burke-Ernzerhof (PBE) was used with a plane wave cutoff of 350 eV [2]. Fermi-Dirac smearing of 0.1 eV was employed for fast convergence, and the energetics were extrapolated to 0 K. All calculations were performed including spin polarization. To sample the Brillouin zone, the number of k points for any dimension is set by a floor function $[30/l]$ where l is the length of the dimension. For surface structures, a dipole correction was applied in the direction normal to the surface. Convergence of self-consistent field (SCF) calculations were achieved when the energy difference between the last three steps is less than 0.0001 eV/electron.

S-3 Details of momentum tensor potentials

In spirit to finite-ranged machine learning potentials, momentum tensor potential (MTP) defines the total energy E as the sum of contributions of local chemical environments ($V(\mathbf{n}_i)$). The atomic local contribution $V(\mathbf{n}_i)$ is expanded by a linear combination of basis functions. Each of the basis function is a contraction of moment tensor descriptors to yield scalars. The moment comprises of two components—one component is a radial function to control the finite-ranged two-body interactions, and the other component is tensor of a certain rank encoding angular information of the atomic environment. By definition, the as-built basis functions preserve the rotation, permutation and reflection symmetries. The maximum level of contraction (lev_{max}) allowed defines the functional form of MTP. For high-entropy alloy AlCrFeCoNi, we used $\text{lev}_{\text{max}}=20$ with Chebyshev polynomials as the radial basis functions. The minimum and cutoff distances of interactions were set as 2 and 5 Å, respectively. For five-species materials with $\text{lev}_{\text{max}}=20$, the total number of parameters to be fitted is 1293. For the breakdown of the number of parameters, readers should consult the work by Novikov et al. [3].

S-4 Random forest classifier for single phase formability

Description of features

As mentioned, we built eight features on top of a given chemical composition. Those features consist of atomic size difference (δ), mixing entropy (ΔS_{mix}), mixing enthalpy (ΔH_{mix}), Pauli electronegativity difference ($\Delta \chi$), molar volume (V_m), bulk modulus (K), melting temperature (T_m), and valence electron concentration (VEC). For the last four features, they are obtained by taking the composition-weighted average of the corresponding atomic attributes. The mixing entropy is defined as $\Delta S_{\text{mix}} = -R \sum_{i=1}^n c_i \ln(c_i)$, where R is the ideal gas constant and c_i is the composition of element i . The Pauli electronegativity difference is expressed as $\Delta \chi = \sqrt{\sum_i^n c_i (\chi_i - \bar{\chi})}$, where χ_i and $\bar{\chi}$ are respective electronegativity of element i and the composition-weighted average of electronegativity. The size difference is given by $\delta = 100 \times \sqrt{\sum_i^n c_i (1 - \frac{r_i}{\bar{r}})}$ where r_i and \bar{r} represent the size of atom i and the weighted average of atom sizes, respectively. The mixing enthalpy reads as $\Delta H_{\text{mix}} = 4 \sum_{i=1}^n \sum_{j>i}^n H_{ij} c_i c_j$, where the binary interaction term is calculated based on the Miedema model [4].

The size, melting temperature, valence electron concentration and molar volume of each element are retrieved from the ‘mendeleev’ python package. The bulk modulus of each element is excerpted from the plot on [the website for periodic table](#) using [WebPlotDigitizer](#). For some missing

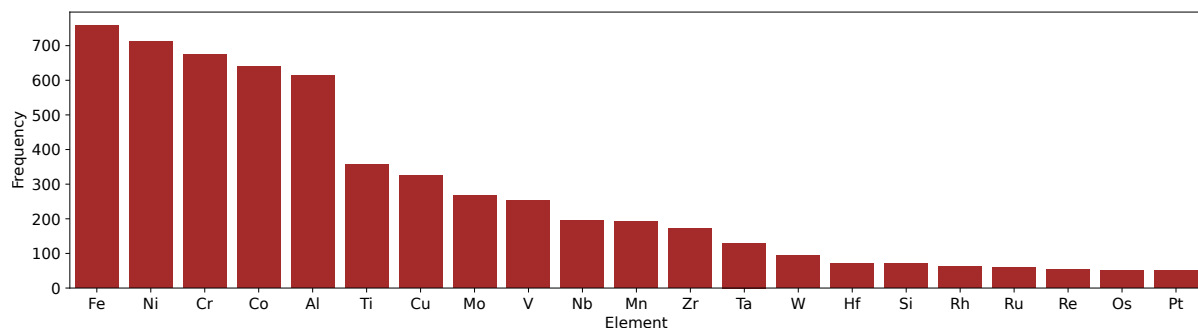


Figure S1: Frequency of elements in the experimental dataset.

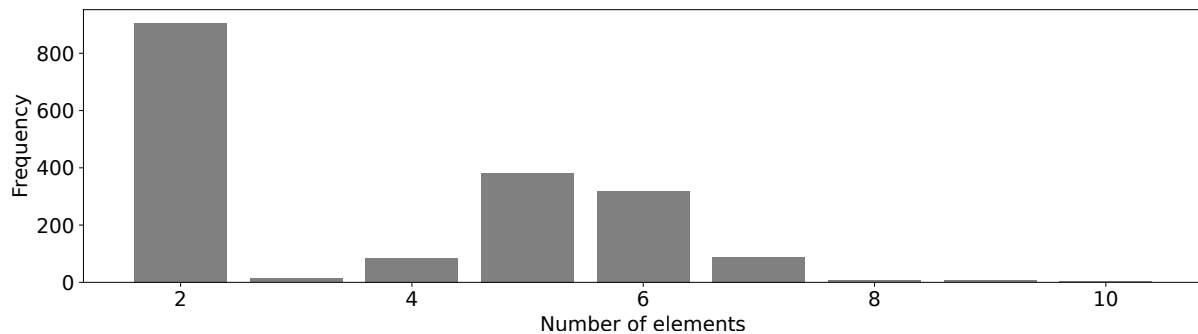


Figure S2: Frequency of number of elements in the experimental data.

bulk modulus and electronegativity values, web values were used. The Midema model calculations were carried out using ‘[qmpy](#)’ python package.

Exploratory data analysis

Figure S1 shows the frequency of elements found in the experimental data. It is clear that the most commonly used five elements are Fe, Ni, Cr, Co and Al, and those noble metals such as Pt and Au are barely used.

Figure S2 summarizes the number of elements for each alloy in the experimental dataset. Most of the alloys are binary and most high-entropy alloys are with five or six elements.

Figure S3 shows the class-wise distribution of values for each feature. A glimpse of these box plots indicate that there are no strong linear dependence of single phase formability with any specific features, implying that non-linear models are needed to describe the complex interactions between feature and output labels.

Model parameters

We built the random forest model using scikit-learn python package (<https://scikit-learn.org/stable/>). We set the number of estimators (decision trees), max depth of each estimator, minimum samples to be split as 100, 20 and 4, respectively. A ‘minmax’ scaler was utilized to scale feature values to the range between -1 and 1 because all feature values are well bounded.

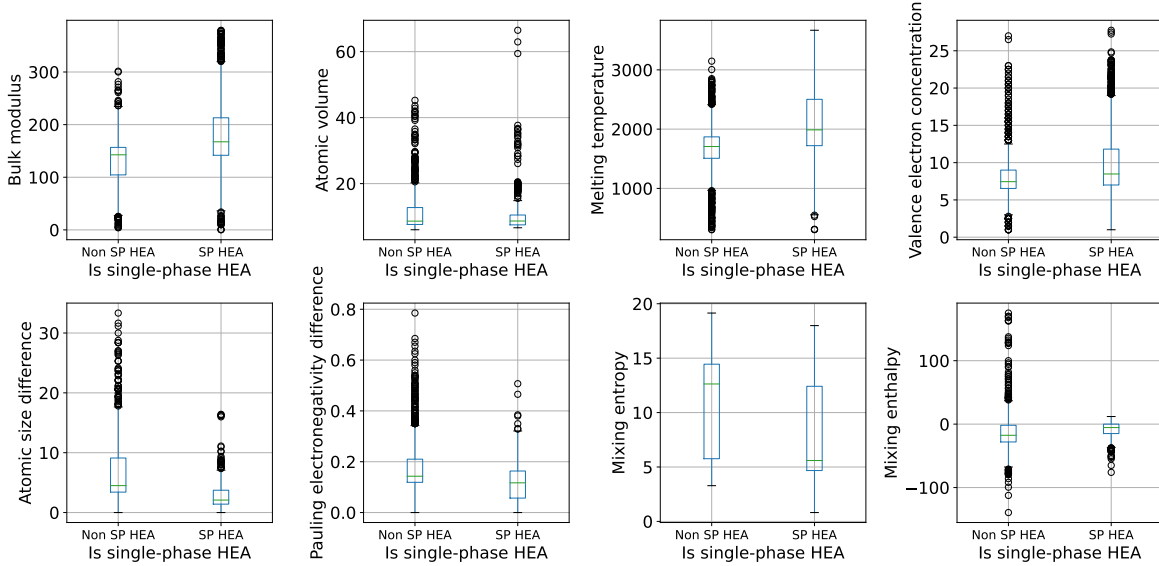


Figure S3: Class-specific feature value distributions.

S-5 Fast sampling of configurations using EAM

To facilitate the process of generation of training structures, we first created bulk FCC structures with a supercell of $3 \times 3 \times 3$ (108 atoms) for $\text{Al}_x(\text{CrFeCoNi})_{100-x}$ with Al compositions being 0, 5, 10, 15 and 20%. The atoms in the supercell were randomly distributed. We performed relaxation using LAMMPS to optimize the lattice geometry and atomic positions at the same time. Starting with the relaxed structures, we performed NVT molecular dynamic (MD) simulations using Langevin dynamics at a temperature of 1700 K, a friction coefficient of 0.002 and time step of 5 fs. 5000 MD steps were carried out and 100 images for each Al composition were saved, out of which 25 structures were selected using a farthest point sampling algorithm to be reevaluated by First-principles calculations. Moreover, we performed Markov chain Monte-Carlo (MCMC) simulations to sample more diverse structures. MC simulations were performed with canonical ensemble at a temperature of 500 K. At each MC step, two neighboring atoms with different types are exchanged and a new structure is created. The new structure is accepted if the potential energy drops; otherwise, it will be accepted with a Boltzmann probability if the potential energy increases. Numbers of MC steps were chosen to ensure that on average at least 40 times of swap were performed for each atom in the system. For each Al composition, 50 MC structures were randomly selected for DFT evaluation. The MD and MC simulations were conducted with Atomic Simulation Environment (ASE) [5] and using the ASE-MTP interface available at [ASEMTP](#). For FCC(111) surfaces, atomic structures with a supercell of $5 \times 5 \times 5$ were created for each Al composition. The same procedure as the sampling for bulk structures was carried out to sample diverse surface structures.

Table S2: Breakdown of the training data.

Data type	Number of training data	Number of atoms
Bulk, relaxation	150	108
Bulk, MD	99	108
Bulk, MCMC	242	108
Bulk, simple	365	1–5
Surface, relaxation	234	125
Surface, MD	99	125
Surface, MCMC	242	125
Surface, simple	138	5
Total	1569	NA

S-6 First-principles data used to construct MTP

We carried out first-principles calculations to refine the properties (energy and forces) of the structures sampled using EAM. Together with the simple bulk structures and surface structures with numbers of elements from one to five, in total 1569 first-principles data were curated. Numbers of training data per simulation task were given in Table S2. High-throughput DFT calculations were operated using methods developed in our previous work [6].

S-7 MTP-enabled simulations used to calculate corrosion metrics

To obtain the results shown in Figure 2, for each Al composition of $\text{Al}_x(\text{CrFeCoNi})_{100-x}$, we create FCC_A1 and L1₂ structures using a supercell of $5 \times 5 \times 5$ (500 atoms), and B2 structures using a supercell of $7 \times 7 \times 7$. We then optimized those structures in ASE using a force stopping criterion of 0.05 eV/Å. As the number of atoms for FCC and BCC structures are different, we cannot directly compare the total energies. Instead, we compare the cohesive energies as shown in Figure 2.

To obtain the values of PBR_{Cr} as shown in Figure 3(b), we created L1₂ structures with systematically varied Al and Cr compositions for $\text{Al}_x\text{Cr}_y(\text{FeCoNi})_{100-x-y}$ using a composition interval of 5%. We performed the structure optimization to find the stable lattice cell and atomic positions. We found linear dependences of lattice constants with both Al and Cr compositions. The fitted coefficients for Al and Cr compositions are respectively $3.26672181\text{e-}03$ and $6.81928982\text{e-}05$, respectively, suggesting a stronger dependence on Al compositions. Therefore, for any pair of Al and Cr for $\text{Al}_x\text{Cr}_y(\text{FeCoNi})_{100-x-y}$, we can find the geometry, hence the volume of Cr element in the alloys. The volume of Cr will be used to calculate PBR_{Cr} .

In order to calculate the surface energies as shown in Figure 3(c), the bulk systems involved are the L1₂ structures used for PBR_{Cr} while for the surface structures, we created a $20 \times 20 \times 5$ (2000 atoms) surface cell to ensure that the periodicity in the surface directions will not affect the arrangement of atoms. We performed MCMC simulations with around 80000 MC steps and a temperature of 500 K to identify stable structures. The surface energies were calculated by taking the difference between energies of surface systems and bulk systems, following by a division over

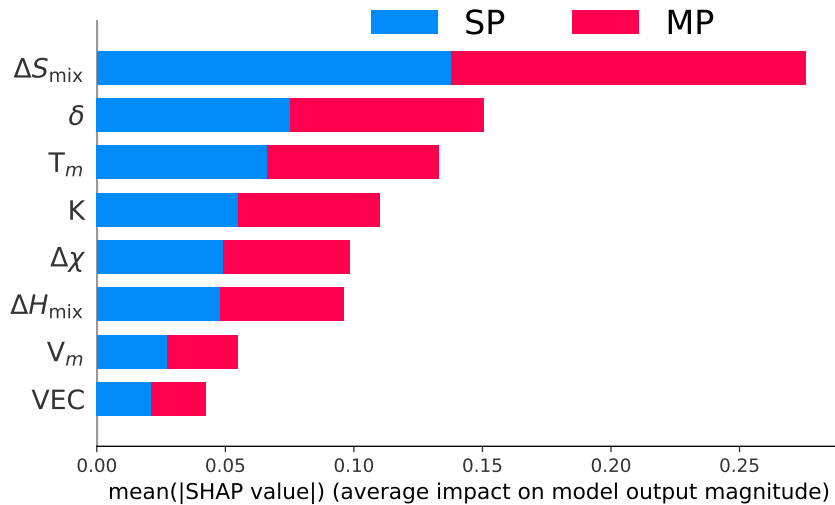


Figure S4: Class-specific shapley feature importance for the trained random forest classifier. SP and MP represent single phase and multiple phase, respectively.

the surface area.

S-8 Supporting results

Feature importance for random forest classifiers

With the random forest classifier, we analyzed the importance of all features using shapley values. The results are plotted in Figure S4. The most important two features are mixing entropy and atomic size difference. The importance of mixing entropy is twofold and competitive. On one hand, thermodynamically high entropy will encourage the system to be well mixed to reduce the Gibbs free energy. On the other hand, mixing more elements tend to be more difficult because there is larger chance attributes among some elements can be highly varied. The importance of atomic size difference is in alignment with intuition that mixing elements with different sizes is more challenging. Interestingly, the least important feature is valence electron concentration although VEC can be good indicator of which type of single phase structures will be formed [7].

Single crystal phase stability as predicted by MTP

We compare the phase stability of two types of single crystals (L1₂ and B2) in the composition space of $\text{Al}_x\text{Cr}_y(\text{FeCoNi})_{100-x-y}$. One should note that the actual state for a given composition can be of multiple phases. The purpose of comparing the energetics of two single phases is to find which type of single phase will form in the actual single-phase regions. The results are shown in Figure S5. At high Cr and Al compositions, BCC-type crystals are more favorable whereas at low Cr and Al compositions, FCC-type crystals are preferential to form.

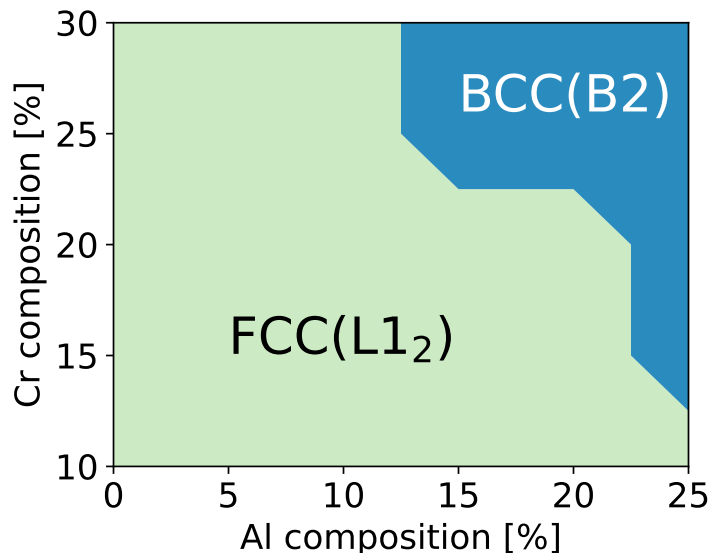


Figure S5: Single crystal phase stability ($L1_2$ versus B2) as a function of Al and Cr compositions.

Surface segregation for Al and Cr

To understand the composition-dependent surface energy, we show the surface segregation of Al and Cr in Figure S6. The surface segregation is defined as:

$$\Delta x_M = c_M^{\text{surface}} - c_M^0 \quad (1)$$

where c_M^{surface} is the surface composition of metal M and c_M^0 is the composition given by the chemical formula. It can be inferred that low-surface energies in the middle and bottom-right regions of Figure 3(c) (marked with a “*” in Figure S6) are results of surface segregation of Al and surface depletion of Cr.

References

- [1] Dohn, A.O.; Jónsson, E.Ö.; Levi, G.; Mortensen, J.J.; Lopez-Acevedo, O.; Thygesen, K.S.; Jacobsen, K.W.; Ulstrup, J.; Henriksen, N.E.; Møller, K.B.; Jónsson, H. Grid-Based Projector Augmented Wave (GPAW) Implementation of Quantum Mechanics/Molecular Mechanics (QM/MM) Electrostatic Embedding and Application to a Solvated Diplatinum Complex. *Journal of Chemical Theory and Computation* **2017**; 13, 6010–6022.
- [2] Perdew, J.P.; Burke, K.; Ernzerhof, M. Generalized Gradient Approximation Made Simple. *Physical Review Letters* **1996**; 77, 3865–3868.
- [3] Novikov, I.S.; Gubaev, K.; Podryabinkin, E.V.; Shapeev, A.V. The MLIP package: moment tensor potentials with MPI and active learning. *Mach. Learn.: Sci. Technol.* **2020**; 2, 025002. Publisher: IOP Publishing.

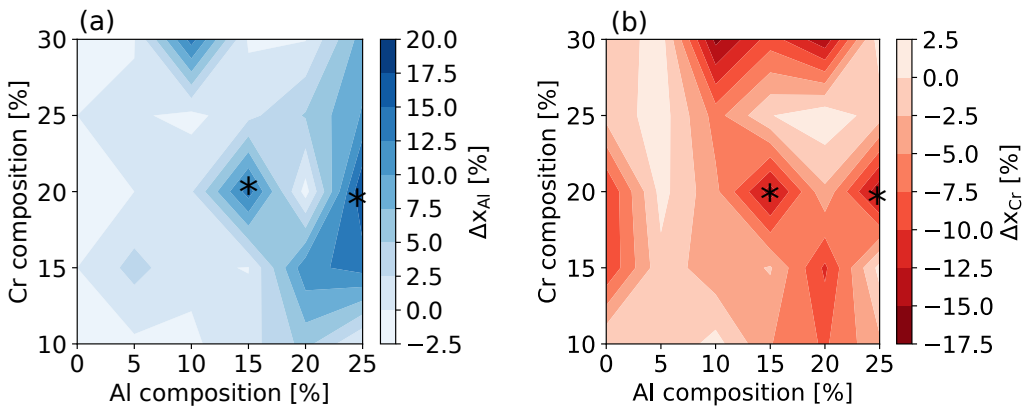


Figure S6: Surface segregation of Al and Cr for different Al and Cr compositions for FCC(111) surfaces of $\text{Al}_x\text{Cr}_y(\text{FeCoNi})_{100-x-y}$.

- [4] Zhang, R.F.; Zhang, S.H.; He, Z.J.; Jing, J.; Sheng, S.H. Miedema Calculator: A thermodynamic platform for predicting formation enthalpies of alloys within framework of Miedema's Theory. *Computer Physics Communications* **2016**; 209, 58–69.
- [5] Hjorth Larsen, A.; Jørgen Mortensen, J.; Blomqvist, J.; Castelli, I.E.; Christensen, R.; Dułak, M.; Friis, J.; Groves, M.N.; Hammer, B.; Hargus, C.; Hermes, E.D.; Jennings, P.C.; Bjerre Jensen, P.; Kermode, J.; Kitchin, J.R.; Leonhard Kolsbjer, E.; Kubal, J.; Kaasbjer, K.; Lysgaard, S.; Bergmann Maronsson, J.; Maxson, T.; Olsen, T.; Pastewka, L.; Peterson, A.; Rostgaard, C.; Schiøtz, J.; Schütt, O.; Strange, M.; Thygesen, K.S.; Vegge, T.; Vilhelmsen, L.; Walter, M.; Zeng, Z.; Jacobsen, K.W. The atomic simulation environment—a Python library for working with atoms. *Journal of Physics: Condensed Matter* **2017**; 29, 273002.
- [6] Zeng, C.; Chen, X.; Peterson, A.A. A nearsighted force-training approach to systematically generate training data for the machine learning of large atomic structures. *The Journal of Chemical Physics* **2022**; 156, 064104.
- [7] Steurer, W. Single-phase high-entropy alloys – A critical update. *Materials Characterization* **2020**; 162, 110179.